



# HST/COS Spectra of the Wind Lines of VFTS 102 and 285

Katherine Shepard<sup>1</sup> , Douglas R. Gies<sup>1</sup> , Kathryn V. Lester<sup>1</sup> , Luqian Wang<sup>1</sup> , Zhao Guo<sup>2</sup> , Lex Kaper<sup>3</sup>,  
Alex De Koter<sup>4</sup>, and Hugues Sana<sup>4</sup>

<sup>1</sup> Center for High Angular Resolution Astronomy and Department of Physics and Astronomy, Georgia State University, P.O. Box 5060, Atlanta, GA 30302-5060, USA; [shepard@astro.gsu.edu](mailto:shepard@astro.gsu.edu), [gies@chara.gsu.edu](mailto:gies@chara.gsu.edu), [lester@astro.gsu.edu](mailto:lester@astro.gsu.edu), [lwang@chara.gsu.edu](mailto:lwang@chara.gsu.edu)

<sup>2</sup> Department of Astronomy and Astrophysics, Pennsylvania State University, 421 Davey Lab, University Park, PA 16802, USA; [zsg124@psu.edu](mailto:zsg124@psu.edu)

<sup>3</sup> Anton Pannekoek Institute for Astronomy, University of Amsterdam, Science Park 904, 1098 XH Amsterdam, The Netherlands; [L.Kaper@uva.nl](mailto:L.Kaper@uva.nl)

<sup>4</sup> Institute of Astrophysics, KU Leuven, Celestijnenlaan 200 D, B-3001 Leuven, Belgium; [A.deKoter@uva.nl](mailto:A.deKoter@uva.nl); [hugues.sana@kuleuven.be](mailto:hugues.sana@kuleuven.be)

Received 2019 September 27; revised 2019 November 14; accepted 2019 November 20; published 2020 January 10

## Abstract

Rapid rotation in massive stars imposes a latitudinal variation in the mass loss from radiatively driven winds that can lead to enhanced mass loss at the poles (with little angular momentum loss) and/or equator (with maximal angular momentum loss). Here we present an examination of the stellar wind lines of the two O-type stars with the fastest known equatorial velocities, VFTS 102 ( $V \sin i = 610 \pm 30 \text{ km s}^{-1}$ ; O9: Vnnne+) and VFTS 285 ( $V \sin i = 609 \pm 29 \text{ km s}^{-1}$ ; O7.5 Vnnn) in the Large Magellanic Cloud. Ultraviolet spectra of both stars were obtained with the *Hubble Space Telescope* Cosmic Origins Spectrograph. The spectrum of VFTS 285 displays a fast outflow in N V and a much slower wind in Si IV, and we argue that there is a two-wind regime in which mass loss is strong at the poles (fast and tenuous wind) but dominant at the equator (slow and dense winds). These ions and wind lines are not present in the spectrum of the cooler star VFTS 102, but the double-peaked H $\alpha$  emission in its spectrum implies equatorial mass loss into a circumstellar disk. The results suggest that in the fastest rotating O-stars, most mass is lost as an equatorial outflow, promoting angular momentum loss that contributes to a spin-down over time.

*Unified Astronomy Thesaurus concepts:* [Stellar winds \(1636\)](#); [Stellar rotation \(1629\)](#); [Massive stars \(732\)](#); [Large Magellanic Cloud \(903\)](#)

## 1. Introduction

Massive stars are hot, luminous objects that experience mass loss by radiatively driven stellar winds (e.g., Puls et al. 2008). Many massive stars are also rapid rotators (e.g., Ramírez-Agudelo et al. 2013); however, despite this commonality, the manner in which rotation affects the wind geometry and mass loss of the star remains a mystery.

Friend & Abbott (1986) and Pauldrach et al. (1986) began to study this problem utilizing calculations that included the effective reduction in gravitational acceleration. This characteristic is a result of the rotational centrifugal acceleration, which reaches its maximum effect at the equator. These models and a subsequent study by Bjorkman & Cassinelli (1993) of the crossing wind trajectory lines over the equator led to the prediction that the effective mass loss rate would increase from pole to equator. However, very rapid rotators are expected to have cooler photospheres closer to their equatorial regions (due to gravity darkening), and further investigations that accounted for cooler equatorial zones and nonradial line forces found that, in fact, the local mass loss rate attains a minimum at the equator (Owocki et al. 1996; Maeder & Meynet 2000; Pelupessy et al. 2000) and that the strongest winds occur at the poles, driving bipolar outflows (Dwarkadas & Owocki 2002; van Boekel et al. 2003; Puls et al. 2008). Detailed wind models by Müller & Vink (2014) confirm that the polar outflows dominate the mass loss, and because the polar gas has little angular momentum, massive stars would lose matter but retain angular momentum, leading to a slower reduction in rotation over time.

Another important factor is the temperature of the photospheric gas and the varieties of ionic transitions that act as wind-driving opacity sources. Vink et al. (1999) showed that as temperatures decline below approximately 25,000 K the ionization balance of

Fe atoms shifts from Fe IV to Fe III, and the multitude of line transitions of the latter act in the winds of B-supergiants to increase dramatically the mass loss rate on the cooler side of a *bi-stability jump*, a point of discontinuity in the properties of stellar winds. Such lower temperatures could exist in the equatorial regions of rapidly rotating stars due to gravity darkening, and Lamers & Pauldrach (1991) showed that in such cases mass loss might be enhanced over these regions (confirmed for differing circumstances by Owocki et al. 1998; Maeder & Meynet 2000; Pelupessy et al. 2000; Madura et al. 2007). This trend was recently and vividly illustrated in wind calculations by Gagnier et al. (2019a), who presented models for the latitudinal variation in wind strength for realistic, two-dimensional models of rapidly rotating O-stars (Espinosa Lara & Rieutord 2011). They found that for very rapid rotation the local temperature may drop below the bi-stability jump, causing a large increase in the local mass loss rate at the equator. The star then enters a two-wind regime with a fast, low-density wind at high latitudes and a slow, very dense outflow near the equator. In this case, the latter component becomes the dominant source of mass and angular momentum loss.

Given the two very different outcomes of the models (polar versus equatorial mass loss), we must seek guidance from observational results for luminous, rapidly rotating stars. The far-ultraviolet spectra of the O-stars are marked by three major resonance doublets—N V  $\lambda\lambda 1238, 1242$ , Si IV  $\lambda\lambda 1393, 1402$ , and C IV  $\lambda\lambda 1548, 1550$ —which are generally formed by scattering in the stellar wind (Howarth & Prinja 1989). These lines appear as P Cygni profiles with blueshifted absorption (from the column of gas carried by the wind projected against the star) and redshifted emission (from the halo of scattered light around the star), and the line strengths and outflow

velocities generally vary according to temperature and gravity associated with the spectral classification (Walborn et al. 1985; Howarth & Prinja 1989). However, the P Cygni lines of several rapid rotators show unusual properties for their classifications. The first case is that of the rapid rotator HD 93521 (O9.5 V;  $V \sin i = 341 \text{ km s}^{-1}$ ). Howarth & Reid (1993) found evidence of both a strong, low-velocity component in the lines of Si IV and C IV and a weaker but high-velocity component in N V and C IV. They interpreted this as the result of a latitudinal dependence in the wind ranging from fast at the poles to slow at the equator. Bjorkman et al. (1994) analyzed the same features and argued for an equatorial wind enhancement through a detailed comparison of the wind line shapes with models (see below). Massa (1995) came to a similar conclusion based upon the strong absorption and weak emission of the lower ionization species that probably form in a denser equatorial region that is seen directly in projection against the stellar disk. Massa (1995) also considered the second example of a rapid rotator,  $\zeta$  Oph (HD 149757; O9.5 Vnn;  $V \sin i = 348 \text{ km s}^{-1}$ ). The N V and C IV lines in its spectrum have strong emission but relatively weak absorption components, which implies that the regions containing these ions do not fully cover the stellar disk and are absent from a dense equatorial zone with lower ionization states seen in partial projection against the star. Prinja et al. (1997) described a third case,  $\gamma$  Arae (HD 157246; B1 Ib), that has a relatively large projected rotational velocity for a supergiant,  $V \sin i = 230 \text{ km s}^{-1}$ . The Si IV lines are strongly in absorption with little emission, in the same way as they appear in the spectrum of HD 93521. Furthermore, there are two sets of migrating discrete absorption components that reach differing outflow speeds, suggestive of an association with both the slower equatorial zone and faster polar region. The last example is the star BI 208 in the Large Magellanic Cloud (O6 V(f));  $V \sin i = 240 \text{ km s}^{-1}$ ; Massey et al. 2009). Massa et al. (2003) noted that the C IV absorption is relatively weak in this star’s spectrum and resembles that of HD 93521, suggesting a wind asymmetry.

The modifications of the appearance of the stellar wind lines in rapid rotators were explored in a seminal paper by Bjorkman et al. (1994). They developed analytical models for line formation in an expanding wind that varies with stellar colatitude. Their model posits a wind with a terminal velocity and local mass loss rate that experiences a transition from a fast polar flow to a slower equatorial flow at an angle corresponding to the half-width of the equatorial disk. The line profiles are found by integration of scattered flux in the wind using an escape probability method and an analytical representation for the wind ionization as a function of distance from the star. The resulting wind line profiles depend upon parameters that describe the geometry and outflows (stellar equatorial velocity, polar and equatorial wind terminal velocities and mass loss rates, the half-width opening angle of the equatorial zone, and the inclination between the spin axis and observer) and the ionization state (different for each line). Bjorkman et al. (1994) present a montage of model profiles for variations in each parameter to demonstrate how these individually influence the final shape of the P Cygni wind profile. Their main result is that the two-component wind model creates an absorption profile shape with a flat “shelf” connecting the deep, low-velocity component to the shallower, high-velocity component that extends to the polar terminal velocity. Their fits of the models to the observed profiles in the spectrum of HD 93521 indicate

that the equatorial density enhancement has a small opening angle, a local mass loss rate about ten times larger than the polar value, and is viewed almost directly edge-on (inclination of  $90^\circ$ ). These models offer important guidance about the interpretation of the P Cygni line profiles in other rapid rotators.

We now have the opportunity to explore the winds of extremely rapid rotators in two cases discovered in the vicinity of the Tarantula Nebula complex in the Large Magellanic Cloud. The Very Large Telescope (VLT)-FLAMES Tarantula Survey (VFTS; Evans et al. 2011) was a large-scale survey to obtain optical spectroscopy of over 800 massive stars in the 30 Doradus region. Among the many remarkable discoveries made in the survey was the identification of two very rapid rotators. Dufton et al. (2011) described the spectrum of VFTS 102, a late-type O-star with  $V \sin i = 610 \pm 30 \text{ km s}^{-1}$  (Ramírez-Agudelo et al. 2013), the largest projected rotational velocity ever measured for this class of stars. A second fast rotator was discovered by Ramírez-Agudelo et al. (2013), VFTS 285, with  $V \sin i = 609 \pm 29 \text{ km s}^{-1}$ . These two fast rotators are conspicuous outliers in the  $V \sin i$  distribution of the VFTS sample, where the majority of single O-type stars have  $V \sin i$  between 40 and  $120 \text{ km s}^{-1}$  (see Figures 5 and 11 in Ramírez-Agudelo et al. 2013). The cause of such rapid rotation in these two stars is unknown. Dufton et al. (2011) discuss the possible origin of VFTS 102 as a star spun-up by mass accretion in a binary system that subsequently broke apart upon the supernova explosion of the companion, which created the nearby X-ray pulsar, PSR J0537–6910. Alternatively, Jiang et al. (2013) and de Mink et al. (2014) describe how a short-period binary might evolve into a contact system that eventually merges to become a single, rapidly rotating star.

These two extremely rapid rotators are ideal targets in which to explore the wind properties in the case of close to critical rotation, where the equatorial velocity is nearly equal to the Keplerian orbital velocity. Here we present spectra of the N V and Si IV profiles of VFTS 102 and 285 obtained with the *Hubble Space Telescope* (HST) and Cosmic Origins Spectrograph (COS). The observations and data reduction are discussed in Section 2. The wind lines contain components formed in the interstellar medium (ISM) of the Galaxy and LMC, and in Section 3 we describe our method to isolate and remove these ISM components. Then in Section 4 we investigate the wind line morphology in the context of the wind lines of Galactic rapid rotators that were observed with the *International Ultraviolet Explorer* (IUE). Our results are summarized in Section 5.

## 2. HST/COS Spectroscopic Observations

The COS is a high-dispersion spectrograph that was designed to record the UV spectra of faint point sources (Green et al. 2012; Fischer 2019). The observations reported here were made during Cycle 23 under program GO-14246. The HST/COS observations of VFTS 102 were obtained over three orbits on 2017 January 1, and those of the brighter VFTS 285 were made in a single orbit on 2016 April 10. These far-UV spectra were all made with the G130M grating in order to record the spectrum over the range from 1150 to  $1450 \text{ \AA}$  with a spectral resolving power of  $R = \lambda/\Delta\lambda = 18,000$ . There are two COS detectors, which are separated by a small gap; therefore the VFTS 102 spectra were made at three slightly different central wavelengths (1300, 1309, and  $1318 \text{ \AA}$ ) in order to fill in the missing flux. In each of these settings, four sub-exposures were

**Table 1**  
Other LMC Stars Observed with COS G130M

Name	Other Name	Spectral Class.	References	$B - V$	No. Spectra	<i>HST</i> Prog.	PI	Used
AAΩ 30 Dor 187	UCAC3 42-30814	O6 (f)np	(1)	−0.18	4	14683	J.-C. Bouret	Y
AAΩ 30 Dor 333	CPD-69° 471	O2−3 (n)fp	(1)	+0.10	8	14683	J.-C. Bouret	Y
AAΩ 30 Dor 368	UCAC3 42-33014	O7.5 (f)np	(1)	−0.12	4	14683	J.-C. Bouret	N
HD 38029	Brey 67	WC4 + OB	(2)	+0.15	1	12581	J. Roman-Duval	N
SK-68° 129	W61 27-56	B1 I	(3)	+0.03	2	12581	J. Roman-Duval	Y
SK-68° 140	VFTS 696	B0.7 Ib–Iab Nwk	(4)	+0.10	1	12581	J. Roman-Duval	N
SK-68° 155	UCAC2 1934920	O8 Ia	(5)	−0.01	1	12581	J. Roman-Duval	Y
SK-69° 279	UCAC2 1677771	O9.2 Iaf	(6)	−0.06	1	12581	J. Roman-Duval	N
VFTS 352	OGLE BRIGHT-LMC-ECL-9	O4.5 V + O5.5 V	(7)	−0.10	16	13806	H. Sana	N
VFTS 102	UCAC2 1803231	O9: Vnnne+	8	+0.35	(1)	14246	D. Gies	...
VFTS 285	...	O7.5 Vnnn	(8)	−0.06	1	14246	D. Gies	...

**Note.** References for classifications: (1) Walborn et al. (2010); (2) Neugent et al. (2018); (3) Massey et al. (2000); (4) Evans et al. (2015); (5) Misselt et al. (1999); (6) Gvaramadze et al. (2018); (7) Abdul-Masih et al. (2019); (8) Walborn et al. (2014).

obtained at four FP-POS, or focal plane offset positions, in order to avoid fixed-pattern problems. The VFTS 285 spectra were made in the same way except only two central wavelength positions were selected, 1300 and 1318 Å, due to orbital time restrictions.

The observations were processed with the standard COS pipeline to create wavelength- and flux-calibrated spectra as `x1d.fits` files for each central wavelength arrangement (Rafelski et al. 2018). The sub-exposures were subsequently merged onto a single barycentric wavelength grid using the IDL procedure `coadd_x1d.pro`<sup>5</sup> (Danforth et al. 2010). Finally, both spectra were transformed to a uniform grid with a  $\log \lambda$  pixel spacing equivalent to a step size in Doppler shift of  $2.60 \text{ km s}^{-1}$  over the range from 1150 to 1440 Å. The coadded spectra have a signal-to-noise ratio of  $S/N = 5$  per pixel in the central, best exposed regions.

The spectra are composed of very broad and blended photospheric lines, very strong  $\text{Ly}\alpha$  absorption, the N V and Si IV wind lines, and numerous sharp interstellar lines. For the purposes of this work, the spectra were flux-normalized by dividing by the mean flux in the region from 1340 to 1440 Å ( $3.45 \times 10^{-15}$  and  $2.11 \times 10^{-14} \text{ erg cm}^{-2} \text{ s}^{-1} \text{ Å}^{-1}$  for VFTS 102 and VFTS 285, respectively). The shape of the observed continuum flux distribution is unaltered. We will defer a discussion of the rotational line broadening of the photospheric lines to a subsequent paper and concentrate on the wind lines in this work.

### 3. Line Components from the Interstellar Medium

Inspection of the *HST*/COS spectra of VFTS 102 and 285 revealed that the wind lines (especially Si IV) are inscribed with narrow interstellar components formed in both the Galaxy and LMC. In order to analyze the wind lines originating from the star itself, we need to remove the ISM components. We approached this problem by searching the *HST* archive for other COS and G130M grating spectra of luminous stars in the LMC in order to identify the general shapes and strengths of the ISM absorption components. Table 1 lists nine other stars that have spectral observations comparable to those of VFTS 102 and 285. The columns of Table 1 list the target name used in the archive, other name, spectral classification

and source,  $B - V$  color index (Massey 2002; Zaritsky et al. 2004; Bonanos et al. 2009; Evans et al. 2011; Zacharias et al. 2013), the number of available COS spectra, the *HST* program number and principal investigator, and whether or not (Y = yes or N = no) the target spectra were used in our scheme to remove the ISM lines. Similar data are given for the two primary targets at the bottom of Table 1. These spectra were reduced to the same wavelength grid using the methods applied to the VFTS 102 and 285 spectra, and where multiple spectra were available, they were coadded to form a single, high-S/N spectrum. We further smoothed the spectra by convolution with an 11 pixel boxcar function, reducing the spectral resolution to  $R = \lambda/\Delta\lambda = 10,000$ . Finally we normalized the spectra to the median average of the flux in the range 1397–1402 Å, leaving the general shape of the spectral energy distribution the same. For our purposes, we restricted this set to four target spectra that display very broad stellar features in the vicinity of Si IV  $\lambda\lambda 1393, 1402$ , so that the narrow ISM lines are readily identified by their sharp appearance. These four spectra are shown in Figure 1, and in all these cases the ISM components appear as narrow absorptions superimposed upon broad P Cygni type profiles. Note that the four selected stars and two primary targets all have similar observed and intrinsic color indices (with the possible exception of VFTS 102, which may appear redder because of the flux contribution from the red continuum of its circumstellar disk; see Section 4.3 below), so we expect that all have similar interstellar column densities.

We used these four spectra to form an average ISM component spectrum<sup>6</sup> for both VFTS 102 and 285. Each spectrum was shifted by a few pixels, allowing the deepest LMC absorption component to align with the same feature in the VFTS target spectra. Then all four were averaged together to form a single spectrum. Next we interpolated across the span of the interstellar components by making parabolic fits of the immediately adjacent line regions. The ISM components were then extracted by dividing by the parabolic fits. The final isolated interstellar lines are shown in the lower portion of Figure 2. The Si IV  $\lambda\lambda 1393, 1402$  profiles of VFTS 102 and

<sup>5</sup> [http://casa.colorado.edu/~danforth/science/cos/coadd\\_x1d.pro](http://casa.colorado.edu/~danforth/science/cos/coadd_x1d.pro)

<sup>6</sup> Note that in principle this averaging should be done by optical depth scaling by first calculating the logarithms of the residual intensities, averaging these, and then forming the exponent of the result. However, because all the ISM components have similar fractional depths for these four stars, the simple average suffices for our purposes.



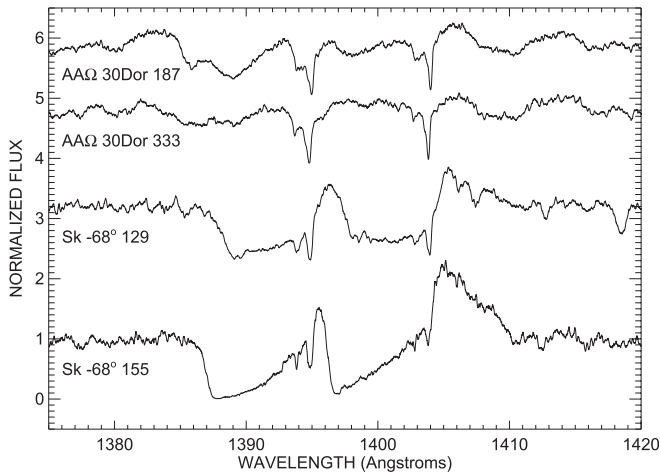


**Figure 1.** *HST/COS* spectra of LMC stars in the vicinity of Si IV  $\lambda\lambda 1393, 1402$ . The ISM components from the Galaxy (left) and LMC (right) are seen as narrow absorptions in both components of the doublet. The normalized fluxes are offset vertically for clarity by +5.3, +4.2, +2.2, and 0 from top to bottom, respectively.

285 are plotted in Figure 2 after smoothing to the same resolving power of  $R = 10,000$ . The gray line corresponds to the observed spectrum and the black line shows the net profiles after subtraction of the ISM lines. In principle, the interstellar absorptions remove a fraction of the flux, therefore technically we should divide rather than subtract their profiles; however, we found that subtraction better preserved the S/N properties of the observed spectra and appeared to succeed in removing most of the interstellar components. We note that the small shifts we applied to align the LMC components may not be appropriate for the Galactic components along the line of sight, but because the Galactic components are relatively weak, this inconsistency has only minor consequences for the subtracted spectra.

The results of ISM removal for the Si IV  $\lambda\lambda 1393, 1402$  lines (Figure 2) show that the spectrum of VFTS 102 has little to no wind contribution in this transition. On the other hand, the ISM-subtracted spectrum of VFTS 285 shows a strong net absorption for both members of the doublet that is Doppler-shifted to a position between the ISM components of the Galaxy and LMC. Such strong features at these wavelengths are not seen in the spectra of any of the other luminous LMC stars listed in Table 1. Therefore, we conclude that this feature has its origin in the star itself. We consider a wind origin for this feature in the next section.

## 4. Wind Profiles of Rapid Rotators

### 4.1. Comparison to a Sample from IUE Spectroscopy

Our intent is to place the appearance (or absence) of the wind profiles in the spectra of VFTS 102 and 285 into the context of the observational properties of wind lines among O-stars in general and rapid rotators in particular. The strengths of the absorption troughs and emission peaks of the wind lines vary as a function of mass loss rate (dependent primarily on luminosity and metallicity), velocity law (often set by exponent  $\beta$  to determine the velocity as a function of radial distance  $r$  by  $v(r) = v_\infty(1 - R_*/r)^\beta$ ), terminal velocity (related to escape velocity), and temperature (related to characteristic ionization fractions). Consequently, the appearance of the wind lines is

closely related to the spectral classification (associated with photospheric temperature and gravity), and there are clear trends with both spectral type and luminosity class. The trends in the primary P Cygni wind lines of N V  $\lambda\lambda 1238, 1242$ , Si IV  $\lambda\lambda 1393, 1402$ , and C IV  $\lambda\lambda 1548, 1550$  for Galactic O-stars are displayed in Figure 2 of the paper by Howarth & Prinja (1989) and additionally in the atlas by Walborn et al. (1985). The N V feature grows in strength and extent (toward larger terminal velocity) from near invisibility among late-type O-stars to dominance among early-type main-sequence stars. Similar trends are observed in giant O-stars, while in supergiants the N V lines are strong among all spectral subtypes. The Si IV line, on the other hand, generally shows only photospheric components (or blends with ISM components) among the O-dwarfs, and wind profiles are only found among the more luminous O-stars (particularly the cooler ones). Crowther et al. (2016) present a similar spectral montage for O-stars in the LMC (see their Figures A1–A11). Although many of the same general trends are present in the LMC O-stars, the wind lines tend to be somewhat weaker than their Galactic counterparts due to the lower metallicity of the LMC and reduced wind-driving line opacities.

The wind lines of rapidly rotating Galactic O-stars show a great diversity of morphology that often departs from the general trends (Howarth & Reid 1993; Massa 1995). Nevertheless, there are patterns among the spectral lines of these rapid rotators that can help place those of the LMC stars in the context of spectral classification and rotational velocity. For this purpose, we collected the available high-dispersion spectra of extremely rapid rotators from the *IUE* archive for a direct comparison of their wind lines with those of VFTS 102 and 285. The stars selected have spectral subtypes from O7 to O9, and are all likely very rapid rotators. Most have large measured projected rotational velocity  $V \sin i$  that is also indicated by one or more “n” labels attached as a suffix to the classification to indicate very broad absorption lines. Several others have an “e” suffix denoting Balmer emission that is usually associated with a circumstellar disk, as found among the rapidly rotating Be stars (Negueruela et al. 2004). Selected stellar parameters for the sample of seven Galactic rapid rotators plus those of VFTS 102 and 285 are summarized in Table 2. The columns list name, number of Short Wavelength Prime, high-resolution spectra from the *IUE* archive, spectral classification and reference, radial velocity and reference, projected rotational velocity and reference, and wind terminal velocity and mass loss rate from the work of Howarth & Prinja (1989). Note that the measured  $V \sin i$  is very large for all the targets except HD 155806, but given the presence of disk-like emission in its spectrum, we expect that it is a rapid rotator viewed from a lower inclination angle with smaller projected rotational Doppler shifts (Negueruela et al. 2004).

We collected all the available spectra of the Galactic rapid rotators from the Mikulski Archive for Space Telescopes (MAST<sup>7</sup>) and transformed these into normalized flux on a uniform  $\log \lambda$  grid. If more than one spectrum was available, then we formed an average spectrum to improve the S/N. Finally all the spectra (*IUE* and *HST/COS*) were smoothed to a resolving power of  $R = 7500$  for ease of comparison. The spectra of the Galactic and LMC stars are collected in Figure 3 for both the N V and Si IV transitions. Each spectrum is plotted

<sup>7</sup> <http://archive.stsci.edu/iue/>

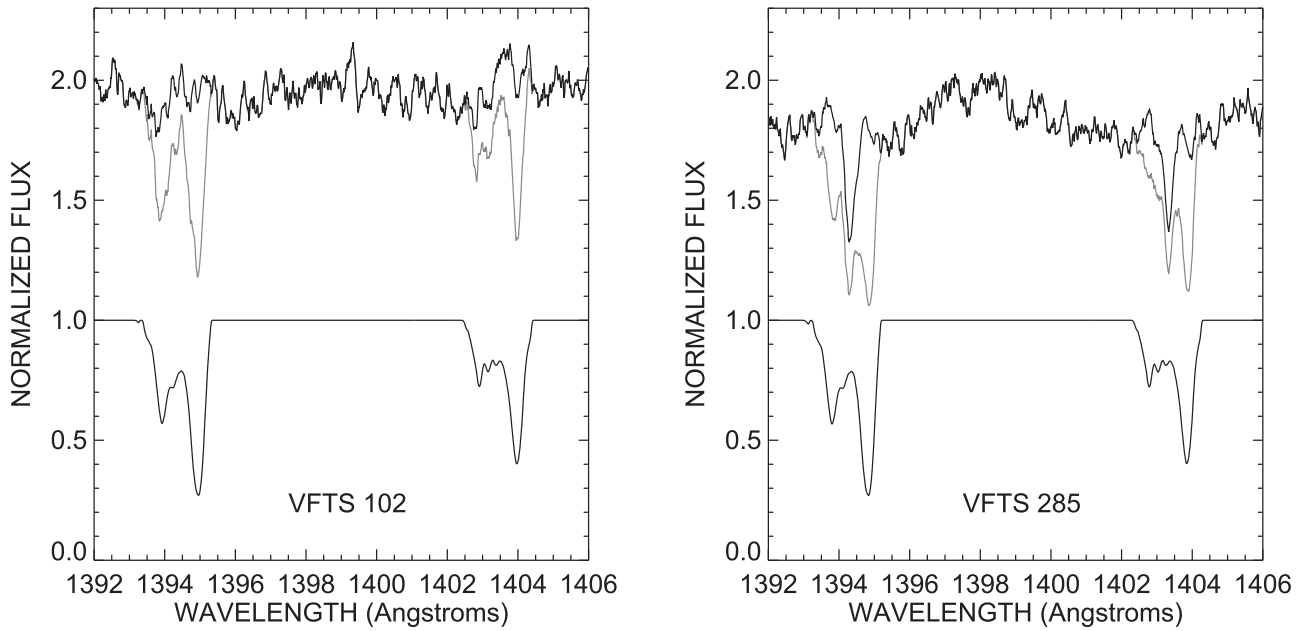


**Figure 2.** *HST*/COS spectra of VFTS 102 and VFTS 285 in the vicinity of Si IV  $\lambda\lambda 1393, 1402$ . The lower solid line shows the expected ISM components for the doublet. The upper lines (offset by +1) depict the observed spectra with both the stellar and interstellar components (gray) and with the ISM components removed (black).

**Table 2**  
Rapidly Rotating O-type Stars

Star Name	No. <i>IUE</i>	Spectral Classification	Reference Code	$V_r$ (km s $^{-1}$ )	Reference Code	$V \sin i$ (km s $^{-1}$ )	Reference Code	$V_\infty$ (km s $^{-1}$ )	$-\log(-dM/dt)$ ( $M_\odot$ yr $^{-1}$ )
HD 46485	2	O7 V((f))n var?	(1)	26	(4)	342	(12)	2250	6.6
HD 60848	12	O8: V:pe	(1)	6	(5)	231	(12)	1650	6.8
HD 93521	150	O9.5 IIIIn	(1)	-14	(6)	341	(12)	1075	7.2
HD 149757	108	O9.2 IVnn	(1)	15	(7)	348	(12)	1640	7.2
HD 155806	4	O7.5 V((f))(e)	(1)	10	(4)	92	(12)	2900	6.6
HD 191423	1	ON9 II-IIIIn	(1)	-52	(8)	392	(12)	1350	6.6
BD+34 $^\circ$ 1058	1	O8 Vn	(2)	-38	(9)	401	(12)	2315	6.3
VFTS 102	0	O9: Vnnne+	(3)	228	(10)	610	(13)	...	...
VFTS 285	0	O7.5 Vnnn	(3)	228	(11)	609	(13)	1287	...

**References.** (1) Maíz Apellániz et al. (2013); (2) Tovmassian et al. (1994); (3) Walborn et al. (2014); (4) Grunhut et al. (2017); (5) Boyajian et al. (2007); (6) Howarth & Reid (1993); (7) Reid et al. (1993); (8) Mahy et al. (2013); (9) this paper; (10) Dufton et al. (2011); (11) Sana et al. (2013); (12) Penny (1996); (13) Ramírez-Agudelo et al. (2013).

as a function of Doppler-shifted velocity in the target star’s frame of reference according to the stellar radial velocity  $V_r$  listed in Table 2. The stars are ordered from weak and fast winds at the top to strong and slow winds at the bottom. We see that the N V doublet absorption features are found to some extent in all these stars with the sole exception of VFTS 102. The outflow velocities associated with these features are generally fast as expected for main-sequence stars with large escape velocities. However, the spectra of the two stars at the bottom of Figure 3, HD 191423 and HD 93521, both show low apparent velocities in the deepest parts of the profile, with decreasing absorption toward more negative velocities. Some of these trends are reflected in the Si IV lines. Again, VFTS 102 shows no obvious wind features, while the lines appear as a composite of slow and fast components in most of the other stars. The strong absorption component found in the spectrum of VFTS 285 is also apparent among the Galactic rapid rotators plotted in the lower part of Figure 3, and these strong

components are associated with slower outflow (as discussed for the case of HD 93521 by Howarth & Reid 1993; Bjorkman et al. 1994; Massa 1995). In the next subsection, we discuss how these properties may reflect changes in the wind properties with stellar colatitude.

#### 4.2. VFTS 285

The N V  $\lambda\lambda 1238, 1242$  doublet appears in the red wing of Ly $\alpha$  (Figure 3), and it clearly displays the blueshifted absorption and redshifted emission characteristic of wind lines. We measured the radial velocity of the two absorption minima as  $V_r = -1059 \pm 20$  km s $^{-1}$ . Adopting a stellar velocity of  $V_r = +228 \pm 7$  km s $^{-1}$  (Sana et al. 2013) leads to a wind terminal velocity of  $v_\infty = 1287 \pm 21$  km s $^{-1}$  in the star’s frame, which is comparable to the average of  $v_\infty = 1320 \pm 315$  km s $^{-1}$  for O7–8 V stars in the 30 Dor region of the LMC (see Table 6 in Crowther et al. 2016). On the other hand, the Si IV  $\lambda\lambda 1393, 1402$  profile shows shallow

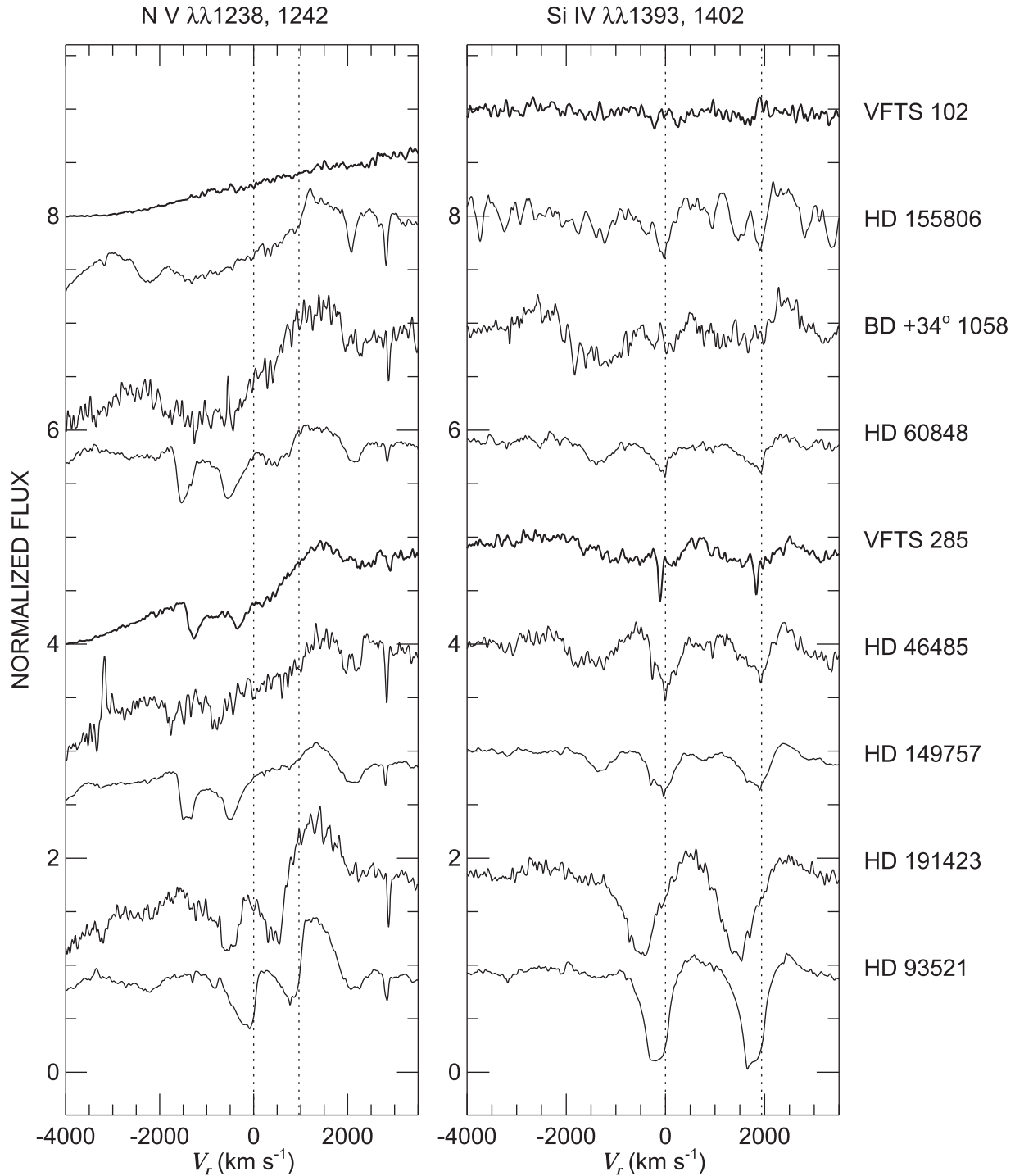


**Figure 3.** The N V  $\lambda\lambda 1238, 1242$  and Si IV  $\lambda\lambda 1393, 1402$  wind line profiles for a sample of *IUE* spectra of Galactic, rapidly rotating, O-stars compared to *HST/COS* spectra of LMC stars VFTS 102 and VFTS 285. Each spectrum is plotted as a function of radial velocity of the blue component of the doublet in the reference frame of the star, and they are offset by integer units of normalized flux for ease of comparison. The rest velocities of each doublet component are indicated by vertical dotted lines.

and weak absorption that extends to similar blueshift, even weaker redshifted emission, and a deep and narrow absorption at a smaller outflow velocity. The minima of the latter component yield a velocity of  $V_r = +121 \pm 10 \text{ km s}^{-1}$ , implying a lower wind outflow velocity of  $v_\infty = 107 \pm 12 \text{ km s}^{-1}$  in the frame of reference of the star. The deep absorption component has a minimum flux that is only  $\approx 12\%$  of the continuum and an FWHM of  $\approx 60 \text{ km s}^{-1}$  in the original COS spectrum before

removal and smoothing of the ISM component. This FWHM is about  $20\times$  smaller than that associated with rotational broadening ( $2 V \sin i$ ), so the feature does not form in the stellar photosphere. Instead, we suggest that the presence of both broad and narrow features in Si IV is indicative of two components in the stellar wind.

We suggest that the differences between the N V and Si IV profiles result from a variation in the wind outflow between the

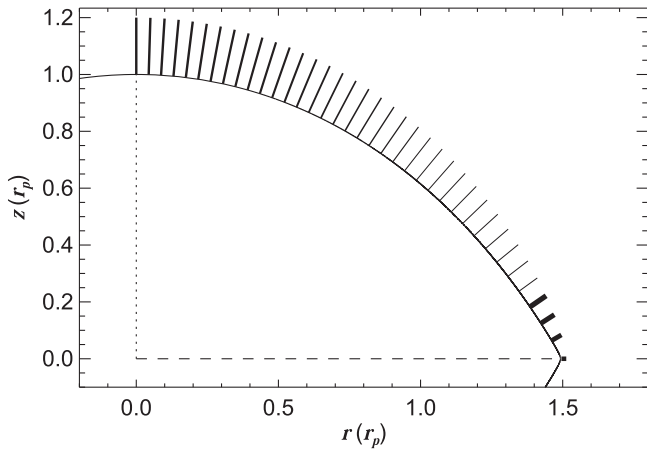


**Figure 4.** The solid line represents a quarter cross section of a very rapidly rotating star such as VFTS 285 for an angular rotation rate of  $\omega = 0.992$  relative to the critical rate. The figure is plotted in terms of cylindrical coordinates for the radial  $r$  and polar  $z$  directions in units of the polar radius  $r_p$ . The dashed and dotted lines represent the equatorial plane and polar axis, respectively. The vectors placed at various surface normals represent the wind velocity (length) and local mass loss rate (thickness) for the two-wind model from Gagnier et al. (2019a). We surmise that the deep, slow absorption in the Si IV profile originates in the strong outflow around the equator and that the faster outflow observed in both the N V and Si IV profiles forms in the regions closer to the pole.

poles and equator and subsequent ionization changes. Gagnier et al. (2019a) present models for the wind variations with colatitude for very rapidly rotating stars that are based upon physically realistic models of the stellar structure and surface temperature variation. We show an example of the shape of a rapidly rotating star in Figure 4 for the case where the ratio of equatorial velocity to Keplerian velocity at the equator is  $\omega = 0.992$ . The shape is defined by the Roche model in which the stellar mass is assumed to be a point source at the center and the outer boundary is set to an equipotential surface defined by the gravitational and centrifugal forces. The temperature varies from hot at the pole to cool at the equator ( $T_{\text{eq}} = 0.55T_{\text{pole}}$  for  $\omega = 0.992$  according to Equation (32) of Espinosa Lara & Rieutord 2011). The mass loss rate reaches a local maximum at the poles due to the intense flux at that point, and declines toward the equator. However, Gagnier et al. (2019a) show that if the gas temperature in the region where the wind originates drops below the bi-stability jump at  $T \approx 25,000$  K, then lower ionization transitions emerge that can act to create a sharp rise in the radiation-driven wind. The result is a two-wind regime in which significant mass loss occurs both at the poles (fast and low density) and at the equator (slow and dense). In the fastest rotators that span the bi-stability jump, the equatorial outflow dominates.

We suggest that the deep and narrow component of the Si IV profile originates in the slow and dense outflow from the equator and that the faster, blueshifted absorption observed in the N V profile forms in the polar winds, which are more comparable to those of slowly rotating main-sequence O-stars. We suspect that the slower, deep absorption component is absent from the N V profile because the gas in the equatorial region is too dense and cool to create highly ionized N. Conversely, the faster, polar outflow is only weakly present in the Si IV profile because Si is ionized beyond  $\text{Si}^{3+}$  in the rarefied and hotter gas of the polar regions.

It is instructive to compare the Si IV profile of VFTS 285 to those model profiles presented by Bjorkman et al. (1994) for the case of the rapid rotator HD 93521. In Section 4.2 of their paper, Bjorkman et al. (1994) show how changes in a given single model parameter from the default set lead to shape differences in the wind line. The transition from a low-velocity, deep absorption (equatorial outflow) to a high-velocity, weaker absorption (polar outflow) creates a mid-range, flat “shelf” in the profile that appears in most of the model profiles. The model profile that most closely resembles the observed Si IV profile is that in their Figure 11 for a total polar optical depth of  $T = 1.0$ , which is less than their default value of  $T = 3.3$  for the Si IV profile formed in the wind of HD 93521. This difference is probably due to the higher photospheric temperature of VFTS 285 that will tend to overionize Si and reduce the optical depth of Si IV in the polar regions. The other difference from the models of Bjorkman et al. (1994) is the observed very narrow appearance of the low-velocity absorption, which we expect is related to the very low effective gravity at the equator and subsequent small terminal velocity (see below). An alternative explanation for the appearance of the Si IV profile might be that we are simply observing a more or less spherical wind in which the optical depth is too low at large distance from the star to create significant absorption at greater blueshift. However, in this case we would expect a smooth transition in profile shape from the low-velocity deeper core to the high-velocity extension (see, for example, the model profiles with low optical depth presented by Castor & Lamers 1979 in their Figure 5). Instead, the sudden transition from steep to shallow slope evident in the profile of Si IV is inconsistent with such spherical models, but is the predicted outcome for two-component winds.

Dwarkadas & Owocki (2002) show how the terminal wind velocity should vary with the local escape velocity at colatitude  $\theta$  according to (their Equation (8))

$$\frac{v_{\infty}(\theta)}{v_{\infty}(0)} = \left[ \frac{g_{\text{eff}}(\theta)}{g_{\text{eff}}(0)} \right]^{1/2}$$

where  $g_{\text{eff}}$  is the local effective gravity. If we suppose that the measured outflow velocities for N V and Si IV correspond to  $v_{\infty}(0)$  and  $v_{\infty}(90^\circ)$ , for the pole and equator respectively, then the relation above can be solved to find

$$\frac{v_{\infty}(90^\circ)}{v_{\infty}(0)} = \left( \frac{r_p}{r_e} \right) (1 - \omega^2)^{1/2}$$

where  $r_p$  and  $r_e$  are the polar and equatorial radii and

$$\omega^2 = \frac{\Omega^2}{GM/r_e^3}.$$

Then for near-critical rotation in which  $r_p/r_e = 2/3$  (Espinosa Lara & Rieutord 2011), we find a normalized rotation frequency of  $\omega = 0.992 \pm 0.002$ , i.e., VFTS 285 is rotating very close to the critical rate of  $\omega = 1$ . Note that this result relies on the assumption that the observed wind velocity measures  $v_{\infty}$ . If, for example, line formation occurs predominantly in denser gas closer to the star where the flow has not reached terminal velocity, then our estimate of  $\omega$  would be an upper limit.

The extremely large projected rotational velocity of VFTS 285 also suggests near-critical rotation. Sabín-Sanjulián et al. (2017)



estimate that the star has a mass  $M/M_{\odot} = 20.1 \pm 0.9$  and radius  $R/R_{\odot} = 6.60 \pm 0.75$ . The projected rotational velocity is so large that it is safe to assume that the inclination is  $i \approx 90^{\circ}$  and  $\sin i \approx 1$ , and thus  $V \sin i \approx \Omega r_e = 1.5 \Omega r_p$ . Setting the adopted radius to  $r_p$  then yields  $\Omega = (8.8 \pm 1.1) \times 10^{-5} \text{ s}^{-1}$  and a rotation period  $P = 2\pi/\Omega = 19.7 \pm 2.5 \text{ hr}$ . The Keplerian angular rotational velocity is  $\Omega_K = \sqrt{GM/r_e^3} = (9.0 \pm 1.6) \times 10^{-5} \text{ s}^{-1}$ , so the estimated ratio is  $\omega = \Omega/\Omega_K = 0.98 \pm 0.08$ . This is the same within uncertainties as that from the previous paragraph found by comparing the difference in wind speed between pole and equator. Thus, VFTS 285 must represent a case of a star very close to critical rotation and oriented with its equator directly along the line of sight ( $i \approx 90^{\circ}$ ), which allows the slow, dense equatorial wind, viewed projected against the star, to appear in the low-velocity, blueshifted absorption component of the Si IV profile.

### 4.3. VFTS 102

There is no evidence of a P Cygni wind profile for either the NV or Si IV transitions in the spectrum of VFTS 102 (Figure 3). This is not unexpected given the O9 V classification of the star. The cooler, late subtype O-stars show little evidence of wind features in these transitions among main-sequence stars in the Galaxy (Walborn et al. 1985; Howarth & Prinja 1989) and in the LMC (Crowther et al. 2016), due to their relatively lower mass loss rates and cooler photospheres. However, the O9 V stars usually show photospheric components of Si IV that are very weak or absent in the spectrum of VFTS 102. We suspect that their absence is partially due to the extremely large projected rotational velocity, which causes all the photospheric lines to appear very broad and shallow. It is also possible that our removal scheme for ISM lines may have inadvertently subtracted out any minor Si IV components from the star. The lack of deep and narrow Si IV components like those observed in the spectrum of VFTS 285 is puzzling given the rapid rotation of VFTS 102. However, since VFTS 102 is cooler, its equatorial outflow may only sustain lower ionization stages of Si, rendering it invisible in the Si IV transitions. A similar situation exists in the cooler Be stars with outflowing disks. Grady et al. (1987) found that wind components of Si IV are sometimes observed in rapidly rotating Be stars (see below), but these are rare in those Be stars with high inclination, presumably because their dense, cooler disks, seen in projection against the star, harbor lower ionization states.

Evidence that the star is losing mass from the equatorial region comes from the Balmer emission lines that place VFTS 102 in the Oe category. We show in Figure 5 the  $H\alpha$  emission line as observed with the VLT X-shooter spectrograph (Vernet et al. 2011) on 2013 November 9. The line appears double-peaked with a central narrow emission component that results from incomplete removal of the surrounding nebular emission. Such double peaks are generally interpreted as forming in a circumstellar decretion disk like those found around classical Be stars (Rivinius et al. 2013). The  $H\alpha$  emission line is particularly strong in the spectrum of VFTS 102 with an equivalent width of  $-42 \pm 2 \text{ \AA}$  and emission peaks reaching to four times the continuum flux level above the continuum (after removal of the nebular component). We used the equivalent width and the method presented by Grundstrom & Gies (2006) to derive a disk half-light radius for  $H\alpha$  emission that is approximately nine times larger than the stellar mean radius, although we caution that this estimate is based upon an extrapolation to higher

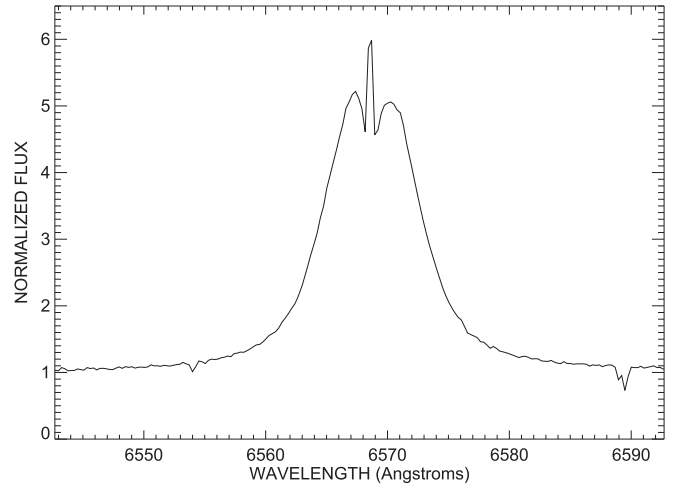


**Figure 5.** X-shooter spectrum of the  $H\alpha$  profile of VFTS 102 that shows double-peaked emission from a large circumstellar disk.

temperature of model results for Galactic abundance stars. In any case, the extremely large  $H\alpha$  emission strength demonstrates that the star is losing mass preferentially through an equatorial flow into a dense and extended circumstellar disk.

## 5. Conclusions

The LMC stars VFTS 102 and 285 are the record-holders for fastest equatorial rotational velocity, and the *HST*/COS spectra of these stars offer us a rare opportunity to observe how rapid rotation affects their radiatively driven mass loss. The wind lines in the spectrum of VFTS 285 show evidence of both a fast outflow that is typical of main-sequence O-stars and a striking and unusual slow component visible in the Si IV  $\lambda\lambda 1393, 1402$  profiles. We argue that these features support the two-wind regime model for very rapid rotators presented by Gagnier et al. (2019a). In this model the wind mass loss rate is high and the speed fastest in the polar regions where the stellar temperature and local escape velocity reach maximum. However, in the case of very rapid rotation, the equatorial zone becomes cool enough that the atmospheric temperature falls below the bi-stability jump where new, low-ionization absorbers help drive a dense and slow outflow. We show that there are similar slow outflow components in the Si IV wind lines of some Galactic rapid rotators, such as HD 93521 and HD 191423, although their outflows are not as slow as that in VFTS 285, presumably as a result of their slower rotation rates and the smaller difference in gravity between the poles and equator.

There is little or no evidence of P Cygni type wind profiles for the cooler star VFTS 102, which is likely due to the lower ionization conditions of its photosphere. On the other hand, there is strong and double-peaked  $H\alpha$  emission in the optical spectrum that demonstrates the presence of an extended circumstellar disk, which is probably the result of mass loss from the equatorial region that carries away the highest amount of angular momentum. The fact that a large disk is present in the cooler star VFTS 102 but absent from the hotter VFTS 285 supports the idea that the intense flux of hotter stars tends to ablate away gas in a circumstellar disk (Kee et al. 2016).

These two cases show that although a two-wind regime may exist in a very rapidly rotating star, observing the spectral signature of the slower equatorial outflow depends upon several conditions: the polar temperature, how close the star is to



critical rotation ( $\omega = 1$ ), the spatial variation of ionization states in the wind, and the inclination of the spin axis to our line of sight. The diversity of wind profiles found among Galactic rapid rotators (Figure 3) reflects the differences among these parameters in different stars. We encourage the development of three-dimensional radiative transfer codes (e.g., Hennicker et al. 2018) in order to compute detailed line profiles for stars with wind outflows and ionization levels dependent on colatitude and to test the predictions of the two-wind regime model. It is important to determine the role of equatorial mass loss, because such an outflow removes relatively more angular momentum and can alter the rotational evolution of massive stars (Gagnier et al. 2019b).

We are grateful to Nolan Walborn (deceased) and Denise Taylor of STScI for their aid in planning the observations with *HST*. Support for Program number GO-14246 was provided by NASA through a grant from the Space Telescope Science Institute, which is operated by the Association of Universities for Research in Astronomy, Incorporated, under NASA contract NAS5-26555. Some of the data presented in this paper were obtained from the Mikulski Archive for Space Telescopes (MAST). Support for MAST for non-*HST* data is provided by the NASA Office of Space Science via grant NNX13AC07G and by other grants and contracts. Institutional support was provided from the GSU College of Arts and Sciences.

*Facilities:* *HST* (COS), VLT:Kueyen (X-shooter).

### ORCID iDs

Katherine Shepard  <https://orcid.org/0000-0003-2075-5227>  
 Douglas R. Gies  <https://orcid.org/0000-0001-8537-3583>  
 Kathryn V. Lester  <https://orcid.org/0000-0002-9903-9911>  
 Luqian Wang  <https://orcid.org/0000-0003-4511-6800>  
 Zhao Guo  <https://orcid.org/0000-0002-0951-2171>  
 Hugues Sana  <https://orcid.org/0000-0001-6656-4130>

### References

- Abdul-Masih, M., Sana, H., Sundqvist, J., et al. 2019, *ApJ*, **880**, 115  
 Bjorkman, J. E., & Cassinelli, J. P. 1993, *ApJ*, **409**, 429  
 Bjorkman, J. E., Ignace, R., Tripp, T. M., & Cassinelli, J. P. 1994, *ApJ*, **435**, 416  
 Bonanos, A. Z., Massa, D. L., Sewilo, M., et al. 2009, *AJ*, **138**, 1003  
 Boyajian, T. S., Gies, D. R., Baines, E. K., et al. 2007, *PASP*, **119**, 742  
 Castor, J. I., & Lamers, H. J. G. L. M. 1979, *ApJS*, **39**, 481  
 Crowther, P. A., Caballero-Nieves, S. M., Bostroem, K. A., et al. 2016, *MNRAS*, **458**, 624  
 Danforth, C. W., Keeney, B. A., Stocke, J. T., Shull, J. M., & Yao, Y. 2010, *ApJ*, **720**, 976  
 de Mink, S. E., Sana, H., Langer, N., Izzard, R. G., & Schneider, F. R. N. 2014, *ApJ*, **782**, 7  
 Dufton, P. L., Dunstall, P. R., Evans, C. J., et al. 2011, *ApJL*, **743**, L22  
 Dwarkadas, V. V., & Owocki, S. P. 2002, *ApJ*, **581**, 1337  
 Espinosa Lara, F., & Rieutord, M. 2011, *A&A*, **533**, A43  
 Evans, C. J., Kennedy, M. B., Dufton, P. L., et al. 2015, *A&A*, **574**, A13  
 Evans, C. J., Taylor, W. D., Hénault-Brunet, V., et al. 2011, *A&A*, **530**, A108  
 Fischer, W. J. 2019, *Cosmic Origins Spectrograph Instrument Handbook v11.0* (Baltimore, MD: STScI)  
 Friend, D. B., & Abbott, D. C. 1986, *ApJ*, **311**, 701  
 Gagnier, D., Rieutord, M., Charbonnel, C., Putigny, B., & Espinosa Lara, F. 2019a, *A&A*, **625**, A88  
 Gagnier, D., Rieutord, M., Charbonnel, C., Putigny, B., & Espinosa Lara, F. 2019b, *A&A*, **625**, A89  
 Grady, C. A., Bjorkman, K. S., & Snow, T. P. 1987, *ApJ*, **320**, 376  
 Green, J. C., Froning, C. S., Osterman, S., et al. 2012, *ApJ*, **744**, 60  
 Grundstrom, E. D., & Gies, D. R. 2006, *ApJL*, **651**, L53  
 Grunhut, J. H., Wade, G. A., Neiner, C., et al. 2017, *MNRAS*, **465**, 2432  
 Gvaramadze, V. V., Kniazev, A. Y., Maryeva, O. V., & Berdnikov, L. N. 2018, *MNRAS*, **474**, 1412  
 Hennicker, L., Puls, J., Kee, N. D., & Sundqvist, J. O. 2018, *A&A*, **616**, A140  
 Howarth, I. D., & Prinja, R. K. 1989, *ApJS*, **69**, 527  
 Howarth, I. D., & Reid, A. H. N. 1993, *A&A*, **279**, 148  
 Jiang, D., Han, Z., Yang, L., & Li, L. 2013, *MNRAS*, **428**, 1218  
 Kee, N. D., Owocki, S., & Sundqvist, J. O. 2016, *MNRAS*, **458**, 2323  
 Lamers, H. J. G., & Pauldrach, A. W. A. 1991, *A&A*, **244**, L5  
 Madura, T. I., Owocki, S. P., & Feldmeier, A. 2007, *ApJ*, **660**, 687  
 Maeder, A., & Meynet, G. 2000, *A&A*, **361**, 159  
 Mahy, L., Rauw, G., De Becker, M., Eenens, P., & Flores, C. A. 2013, *A&A*, **550**, A27  
 Maíz Apellániz, J., Sota, A., Morrell, N. I., et al. 2013, in *Massive Stars: From Alpha to Omega*, **198**  
 Massa, D. 1995, *ApJ*, **438**, 376  
 Massa, D., Fullerton, A. W., Sonneborn, G., & Hutchings, J. B. 2003, *ApJ*, **586**, 996  
 Massey, P. 2002, *ApJS*, **141**, 81  
 Massey, P., Waterhouse, E., & DeGioia-Eastwood, K. 2000, *AJ*, **119**, 2214  
 Massey, P., Zangari, A. M., Morrell, N. I., et al. 2009, *ApJ*, **692**, 618  
 Misselt, K. A., Clayton, G. C., & Gordon, K. D. 1999, *ApJ*, **515**, 128  
 Müller, P. E., & Vink, J. S. 2014, *A&A*, **564**, A57  
 Negueruela, I., Steele, I. A., & Bernabeu, G. 2004, *AN*, **325**, 749  
 Neugent, K. F., Massey, P., & Morrell, N. 2018, *ApJ*, **863**, 181  
 Owocki, S. P., Cranmer, S. R., & Gayley, K. G. 1996, *ApJL*, **472**, L115  
 Owocki, S. P., Cranmer, S. R., & Gayley, K. G. 1998, *Ap&SS*, **260**, 149  
 Pauldrach, A., Puls, J., & Kudritzki, R. P. 1986, *A&A*, **164**, 86  
 Pelupessy, I., Lamers, H. J. G. L. M., & Vink, J. S. 2000, *A&A*, **359**, 695  
 Penny, L. R. 1996, *ApJ*, **463**, 737  
 Prinja, R. K., Massa, D., Fullerton, A. W., Howarth, I. D., & Pontefract, M. 1997, *A&A*, **318**, 157  
 Puls, J., Vink, J. S., & Najjarro, F. 2008, *A&ARv*, **16**, 209  
 Rafelski, M., Fox, A., Massa, D., et al. 2018, *COS Data Handbook v4.0* (Baltimore, MD: STScI)  
 Ramírez-Agudelo, O. H., Simón-Díaz, S., Sana, H., et al. 2013, *A&A*, **560**, A29  
 Reid, A. H. N., Bolton, C. T., Crowe, R. A., et al. 1993, *ApJ*, **417**, 320  
 Rivinius, T., Carciofi, A. C., & Martayan, C. 2013, *A&ARv*, **21**, 69  
 Sabín-Sanjulián, C., Simón-Díaz, S., Herrero, A., et al. 2017, *A&A*, **601**, A79  
 Sana, H., de Koter, A., de Mink, S. E., et al. 2013, *A&A*, **550**, A107  
 Tovmassian, H. M., Hovhannessian, R. K., Epremian, R. A., & Huguenin, D. 1994, *MNRAS*, **266**, 337  
 van Boekel, R., Kervella, P., Schöller, M., et al. 2003, *A&A*, **410**, L37  
 Vernet, J., Dekker, H., D'Odorico, S., et al. 2011, *A&A*, **536**, A105  
 Vink, J. S., de Koter, A., & Lamers, H. J. G. L. M. 1999, *A&A*, **350**, 181  
 Walborn, N. R., Howarth, I. D., Evans, C. J., et al. 2010, *AJ*, **139**, 1283  
 Walborn, N. R., Nichols-Bohlin, J., & Panek, R. J. 1985, *NASRP*, **1155**  
 Walborn, N. R., Sana, H., Simón-Díaz, S., et al. 2014, *A&A*, **564**, A40  
 Zacharias, N., Finch, C. T., Girard, T. M., et al. 2013, *AJ*, **145**, 44  
 Zaritsky, D., Harris, J., Thompson, I. B., & Grebel, E. K. 2004, *AJ*, **128**, 1606